

Scalar quantities as detectors of non-Gaussianity on CMB maps

C. Monteserín^{1,2}, R.B. Barreiro^{1,2}, E. Martínez-González¹ and J.L. Sanz¹

¹ *Instituto de Física de Cantabria, CSIC-Universidad de Cantabria, Avda. de los Castros s/n, 39005 Santander, Spain*

² *Dpto. de Física Moderna, Universidad de Cantabria, Avda. de los Castros s/n, 39005 Santander, Spain*

9 September 2018

ABSTRACT

We study the power of several scalar quantities constructed on the sphere (presented in Monteserín et al.) to detect non-Gaussianity on the temperature distribution of the cosmic microwave background (CMB). The test has been performed using non-Gaussian CMB simulations with injected skewness or kurtosis generated through the Edgeworth expansion. We have also taken into account in the analysis the effect of anisotropic noise and the presence of a Galactic mask. We find that the best scalars to detect an excess of skewness in the simulations are the derivative of the gradient, the fractional isotropy, the Laplacian and the shape index. For the kurtosis case, the fractional anisotropy, the Laplacian and the determinant are the quantities that perform better.

Key words: methods: analytical - methods: statistical - cosmic microwave background

1 INTRODUCTION

The cosmic microwave background (CMB) is currently one of the most powerful tools of cosmology. Its study provides us with essential information about the origin and evolution of the Universe. In particular, a key issue is whether the CMB temperature fluctuations follow a Gaussian distribution, as predicted by the standard inflationary model. A detection of intrinsic non-Gaussianity in the CMB would be a hint of new physics (See Bartolo et al. 2004 or Turok & Spergel 1990 and references therein) and therefore would have far reaching consequences on our current knowledge of the Universe. In addition secondary anisotropies (such as the Sunyaev-Zeldovich effects, or the Rees-Sciama effect), contaminant astrophysical emissions (coming from Galactic and extragalactic foregrounds) and systematics can also leave non-Gaussian imprints in the observed microwave sky. Therefore, it is crucial to perform a careful study of any possible detected non-Gaussianity in order to understand its origin.

In the last years there has been a large number of experiments measuring the CMB anisotropies and polarization (DASI, Halverson et al. 2002; VSA, Grainge et al. 2003; CBI, Mason et al. 2003; ACBAR, Kuo et al. 2004; Archeops, Benoit et al. 2003). In particular, the NASA WMAP satellite has provided with high quality observations of the whole sky (Bennett et al. 2003a). Many works have studied the Gaussianity of

the WMAP data, including the use of wavelet tools (Vielva et al. 2004, Mukherjee & Wang 2004, Cruz et al. 2005, Cruz et al. 2006a, Cruz et al. 2006b, McEwen et al. 2005 and Cayón, Jin & Treaster 2005), harmonic techniques (Komatsu et al. 2003, Chiang et al. 2003, Coles et al. 2004, Naselsky, Doroshkevich & Verkhodanov 2004, Magueijo & Medeiros 2004), and real space analyses (Park 2004, Eriksen et al. 2004a, Hansen et al. 2004, Larson & Wandelt 2004, Larson & Wandelt 2005, Cabella et al. 2005), finding in some cases deviations from Gaussianity whose origin is uncertain. In this paper, we are interested in the study of the Gaussianity of the CMB using a set of scalar quantities of the temperature field, such as the Laplacian, the shape index or the Gaussian curvature. Previous works on related methods include the study of maxima properties (Bond & Efstathiou 1987, Barreiro et al. 1997, Gurzadyan & Torres 1997, Barreiro, Martínez-González & Sanz 2001), the fraction of lake and hill points (Doré, Colombi & Bouchet 2003, Cabella et al. 2005) or the skeleton length (Novikov, Colombi & Doré 2006, Eriksen et al. 2004b).

Some previous works have also compared the performance of different statistics to detect non-Gaussianity in the CMB using a reference set of non-Gaussian simulations. For instance, Hobson et al. (1999) compared the capability of wavelet techniques and Minkowski functionals as non-Gaussianity detectors using simulated maps of the Kaiser-Stebbins effect. The comparative performance of the Spher-

arXiv:astro-ph/0604356v3 3 Jul 2006

ical Haar Wavelet and the Spherical Mexican Hat Wavelet has been tested on non-Gaussian simulations generated through the Edgeworth expansion (Martínez-González et al. 2002). Aghanim et al. (2003) studied the relative performance of wavelet and Fourier based methods by applying them to three different sets of non-Gaussian maps that were representative of possible non-Gaussian signatures present in the CMB. Three different approaches in pixel, harmonic and wavelet space were tested by Cabella et al. (2004) on simulations of the quadratic potential model and on Gaussian maps contaminated by point sources. Jin et al. (2005) have compared theoretically and experimentally the performance of the kurtosis to the Higher Criticism and MAX statistics in the wavelet and curvelet spaces.

In a previous work, Monteserín et al. (2005) (hereafter M05) studied the probability distribution of a series of scalar quantities assuming that the CMB is a homogeneous and isotropic Gaussian field and including also the effect of anisotropic noise and the presence of a mask. These quantities were proposed as promising tools for the analysis of the temperature distribution of the CMB. In the present paper, we study the performance of these scalars (as well as three new ones) to detect non-Gaussianity in the CMB. In particular, we have tested the method using non-Gaussian simulations with skewness and kurtosis injected through the Edgeworth expansion (Martínez-González et al. 2002). Although Edgeworth simulations do not correspond to a realistic model, it is expected that physical motivated models, as well as contaminant emissions, will introduce a certain level of skewness and/or kurtosis in the CMB distribution. As an example, the quadratic potential model would introduce skewness in the CMB (Komatsu & Spergel 2001), the cosmic strings would generate kurtosis (Hobson, Jones & Lasenby 1999, Barreiro & Hobson 2001) whereas residual point sources would introduce both (Argüeso et al. 2006). Therefore the use of non-Gaussian simulations constructed through the Edgeworth expansion, where a certain level of skewness or kurtosis is injected, provides us with an interesting tool in order to test the type of deviations from Gaussianity that one would expect in realistic data.

The article is organised as follows. In §2 we briefly summarise the work of M05, describing the different considered scalars (including three new quantities) and presenting some theoretical results for the case of a Gaussian field. Our simulations are described in §3 whereas §4 presents the results of our Gaussianity test. Section §5 summarises our main conclusions. Finally, we include a series of appendices with the description of the three new quantities as well as analytical expressions for the cumulative functions of some of the considered scalars.

2 SCALARS ON THE SPHERE

The temperature anisotropies of the CMB are usually described as a 2-dimensional field $T(\theta, \phi)$ on the sphere. The first and second derivatives of the field encode very interesting information about the fluctuations. In particular, different quantities which are scalars under a change of the coordinate system (i.e. regular general transformation $(x_1, x_2) \rightarrow (x'_1, x'_2) : s'(x'_1, x'_2) = s(x_1, x_2)$) can be constructed from the first and second covariant derivatives of

the field, which can be useful to perform Gaussian studies of the CMB. Since a field can deviate from Gaussianity in an infinite number of ways, it is a non-trivial task to design a unique set of scalars that is optimal to detect any possible type of non-Gaussianity. Therefore our aim is to study the performance of a (relatively large) number of scalars to detect some generic types of non-Gaussianity (non-zero skewness and kurtosis). In particular, M05 studied the probability density function of different scalars for a homogeneous and isotropic Gaussian field. In this section we briefly describe these quantities (for a more detailed description, see M05) and introduce three new scalars (curvedness, fractional isotropy and fractional anisotropy).

Using first derivatives we can construct the square of the modulus of the gradient g , which provides information on how the temperature varies spatially, and is given by:

$$g = T^{,i}T_{,i} . \quad (1)$$

Other scalars can be constructed using only second derivatives. These scalars are directly related to the eigenvalues λ_i of the negative Hessian matrix of the field, $[-T_{,ij}]$. In particular the eigenvalues can be written as a function of the covariant second derivatives in the following way:

$$\lambda_1 = -\frac{1}{2} \left[(T^{,i}_{,i}) - \sqrt{(T^{,i}_{,i})^2 - 2(T^{,i}_{,i}T^{,j}_{,j} - T^{,ij}_{,i}T^{,ij}_{,j})} \right] \quad (2)$$

$$\lambda_2 = -\frac{1}{2} \left[(T^{,i}_{,i}) + \sqrt{(T^{,i}_{,i})^2 - 2(T^{,i}_{,i}T^{,j}_{,j} - T^{,ij}_{,i}T^{,ij}_{,j})} \right] , \quad (3)$$

Combining these three quantities, we can construct other scalars that enhance different features or properties of the analysed temperature field. An interesting scalar is given by the trace of the Hessian matrix (the Laplacian) λ_+ :

$$\lambda_+ = -\lambda_1 - \lambda_2 . \quad (4)$$

The distortion λ_- and the shear y are related to the difference between eigenvalues:

$$\lambda_- = \lambda_1 - \lambda_2 , \quad (5)$$

$$y = \frac{1}{4}(\lambda_1 - \lambda_2)^2 . \quad (6)$$

While these scalars describe the asymmetry of the field through the difference of the eigenvalues, other scalars express a similar information using their ratio. The ellipticity e and its bounded construction the shape index ι are dimensionless scalars given by:

$$e = \frac{\lambda_1 - \lambda_2}{2(\lambda_1 + \lambda_2)} , \quad (7)$$

$$\iota = \frac{2}{\pi} \arctan \left(-\frac{1}{2e} \right) \quad (8)$$

Other scalars, related to the curvature of the field, are the determinant d of the Hessian matrix, the Gaussian curvature κ_G and the curvedness c (see appendix A):

$$d = \lambda_1 \lambda_2 , \quad (9)$$

$$\kappa_G = \frac{\lambda_1 \lambda_2}{(1 + g)^2} , \quad (10)$$

$$c = \frac{1}{2} \sqrt{\lambda_1^2 + \lambda_2^2} . \quad (11)$$

We can also construct new scalars by combining two of the previous scalars. Examples of these are the fractional isotropy f_i and the fractional anisotropy f_a , which correspond, respectively, to the Laplacian and the distortion weighted by the curvedness (see appendices B and C):

$$f_i = \frac{1}{\sqrt{2}} \frac{\lambda_1 + \lambda_2}{\sqrt{\lambda_1^2 + \lambda_2^2}}, \quad (12)$$

$$f_a = \frac{1}{\sqrt{2}} \frac{\lambda_1 - \lambda_2}{\sqrt{\lambda_1^2 + \lambda_2^2}}. \quad (13)$$

Finally, we have also considered the derivative of the square of the gradient modulus, D_g :

$$D_g = T^{ij} T_{,i} T_{,j}, \quad (14)$$

Assuming that $T(\theta, \phi)$ is a homogeneous and isotropic Gaussian random field, we can derive analytical or semi-analytical expressions for the probability density function (pdf) of the previous scalars (see M05 and appendices A to C). In this case, the pdf of the different scalars is completely determined by the power spectrum, C_ℓ of the original field T . This dependence appears in the distribution function of the scalars through the moments of the initial field, σ_i :

$$\sigma_i^2 = \sum_{\ell} C_{\ell} \frac{2\ell + 1}{4\pi} [\ell(\ell + 1)]^i. \quad (15)$$

However, as shown in M05, it is possible to remove the dependence of the pdf of the scalars on the power spectrum of the field by constructing new quantities that we have called *normalised scalars*. Therefore, for the Gaussian case, a given normalised scalar will have the same distribution function independently of the power spectrum of the field. The definitions of the normalised scalars – as a function of the ordinary scalars – as well as their pdf's for a homogeneous and isotropic Gaussian field are given in table 1 (for completeness we also include the normalised temperature in the table). In addition to its greater simplicity, these new quantities allow us to deal in a straightforward way with the presence of anisotropic noise (see below).

We have to point out that many of the considered normalised scalars have some level of correlation between each other. For a Gaussian field the maximum number of uncorrelated scalars is three, for scalars constructed from the first and second derivatives. In particular, the square of the modulus of the gradient is uncorrelated with all the other scalars. Therefore a set of three uncorrelated scalars will be formed by g and two other scalars, whose choice is not unique. All the information about correlations between the normalised scalars is given in table 2 of M05 and table A1 of this work.

In order to construct the normalised scalars of a field, a necessary step is the calculation of the moments σ_0 , σ_1 and σ_2 given by equation (15) through the C_ℓ 's. For a noiseless CMB map this is trivial provided that we know its power spectrum. However, in the presence of anisotropic Gaussian noise and a mask some further considerations need to be made. Given that the noise and the mask introduce discontinuities in the CMB map, which represents a problem for the calculation of the derivatives, we first filter the considered map with a Gaussian beam of dispersion σ_g (which is chosen to be equal to the dispersion of the beam of the observed CMB map). The anisotropic noise is characterized by a different dispersion at each pixel, $\sigma_n(\vec{x})$ (with \vec{x} the unity

vector on the sphere in the direction of observation). In order to construct the normalised scalars we need to calculate the moments of the field taking into account the different noise in each pixel. This is done using a *pixel dependent power spectrum* $H_\ell(\vec{x})$ (see M05):

$$H_\ell(\vec{x}) = \left[C_\ell^s e^{-\ell(\ell+1)\sigma_g^2} + \frac{4\pi\sigma_n^2(\vec{x})}{N_{pix}} \right] e^{-\ell(\ell+1)\sigma_g^2} \quad (16)$$

where N_{pix} is the total number of pixels of the map. $H_\ell(\vec{x})$, for fixed \vec{x} , corresponds to the power spectrum of a map containing the filtered CMB signal plus isotropic noise with dispersion $\sigma_n(\vec{x})$ and filtered again with a Gaussian beam of dispersion σ_g . Note that, due to this extra smoothing, the dispersion of the noise in a given pixel will depend not only on the noise level on that position but also on the σ_n of its neighbouring pixels. However provided that $\sigma_n(\vec{x})$ varies smoothly, as it is usually the case, this effect is small.

Therefore, using $H_\ell(\vec{x})$, we can obtain the moments of the field $\sigma_i(\vec{x})$ at each pixel and, from them, construct the normalised scalars by introducing these pixel dependent moments on their corresponding definitions. The normalised scalars constructed in this way for a Gaussian initial field will follow the pdf's given in table 1, which are independent of the underlying power spectrum and the level of anisotropic noise.

We would like to point out that if the dispersion of the noise does not vary smoothly along the map, equation (16) may not be a sufficiently good approximation to obtain $\sigma_i(\vec{x})$. In this case, the contribution of the noise to the moments of the field can still be obtained using simulations. Note that since signal and noise are independent, their contributions to $\sigma_i(\vec{x})$ can be calculated separately and then simply added together (quadratically). In order to obtain numerically the contribution of the noise to $\sigma_i(\vec{x})$, we need to generate a large number (1000) of noise simulations, that are smoothed with a Gaussian beam of dispersion σ_g . We obtain then the dispersion of the noise σ_0 in the smoothed map at a given pixel, as the dispersion of the values of the 1000 simulations at that pixel. To obtain $\sigma_1(\vec{x})$ and $\sigma_2(\vec{x})$, we need to construct two ordinary scalars, the square of the modulus of the gradient g and the Laplacian λ_+ , corresponding to the previous smoothed noise simulations. As shown in M05, the mean value of g at each pixel is given by $\sigma_1^2(\vec{x})$ whereas $\sigma_2(\vec{x})$ corresponds to the dispersion of λ_+ at each position. Therefore, by estimating these quantities at each pixel from the ordinary gradient and Laplacian of the smoothed noise simulations, we obtain the contribution of the noise to the moments of the field.

By comparing the estimated values of $\sigma_i(\vec{x})$ using the numerical and analytical (approximated) methods, we can quantify which is the error introduced in these quantities when using the approximated technique. In particular, we have calculated $\sigma_i(\vec{x})$ using both methods for the example considered in this work, which corresponds to the level of noise expected in the Q+V+W combined map of the 4-year WMAP data (see §3). We find that the average error¹ on the calculation of the noise contribution to $\sigma_i(\vec{x})$ is less than 2

¹ This error is defined as $100 \times \left| \frac{\sigma_i^n - \sigma_i^a}{\sigma_i^n} \right| / \sigma_i^n$, where σ_i^n and σ_i^a refer to the i th moment obtained with the numerical and approximated approaches respectively

Normalised scalar	Notation	Definition	Domain	pdf
temperature	\tilde{T}	$\frac{T}{\sigma_0}$	$(-\infty, \infty)$	$p(\tilde{T}) = \frac{1}{\sqrt{2\pi}} e^{-\frac{\tilde{T}^2}{2}}$
greatest eigenvalue	$\tilde{\lambda}_1$	$\frac{1}{2} (\tilde{\lambda}_+ + \tilde{\lambda}_-)$	$(\tilde{\lambda}_2, \infty)$	$p(\tilde{\lambda}_1) = \frac{4}{3\sqrt{2\pi}} e^{-2\tilde{\lambda}_1^2} \left(1 + \sqrt{\frac{2\pi}{3}} \tilde{\lambda}_1 e^{\frac{\tilde{\lambda}_1^2}{3}} \left[1 + \operatorname{erf} \left(\sqrt{\frac{2}{3}} \tilde{\lambda}_1 \right) \right] \right)$
lowest eigenvalue	$\tilde{\lambda}_2$	$\frac{1}{2} (\tilde{\lambda}_+ - \tilde{\lambda}_-)$	$(-\infty, \tilde{\lambda}_1)$	$p(\tilde{\lambda}_2) = \frac{4}{3\sqrt{2\pi}} e^{-2\tilde{\lambda}_2^2} \left(1 - \sqrt{\frac{2\pi}{3}} \tilde{\lambda}_2 e^{\frac{\tilde{\lambda}_2^2}{3}} \left[1 - \operatorname{erf} \left(\sqrt{\frac{2}{3}} \tilde{\lambda}_2 \right) \right] \right)$
Laplacian	$\tilde{\lambda}_+$	$-\frac{\lambda_+}{\sigma_2}$	$(-\infty, \infty)$	$p(\tilde{\lambda}_+) = \frac{1}{\sqrt{2\pi}} e^{-\frac{\tilde{\lambda}_+^2}{2}}$
determinant	\tilde{d}	$\tilde{\lambda}_1 \tilde{\lambda}_2$	$(-\infty, \infty)$	$p(\tilde{d}) = \begin{cases} \frac{4}{\sqrt{3}} e^{4\tilde{d}} & \tilde{d} < 0 \\ \frac{4}{\sqrt{3}} e^{4\tilde{d}} \left[1 - \operatorname{erf} \left(\sqrt{6\tilde{d}} \right) \right] & \tilde{d} > 0 \end{cases}$
shear	\tilde{y}	$\frac{y}{\sigma_2^2 - 2\sigma_1^2}$	$(0, \infty)$	$p(\tilde{y}) = 4e^{-4\tilde{y}}$
distortion	$\tilde{\lambda}_-$	$\frac{\lambda_-}{\sqrt{\sigma_2^2 - 2\sigma_1^2}}$	$(0, \infty)$	$p(\tilde{\lambda}_-) = 2\tilde{\lambda}_- e^{-\tilde{\lambda}_-^2}$
ellipticity	\tilde{e}	$\frac{e\sigma_2}{\sqrt{\sigma_2^2 - 2\sigma_1^2}}$	$(-\infty, \infty)$	$p(\tilde{e}) = 4 \tilde{e} (1 + 8\tilde{e}^2)^{-\frac{3}{2}}$
shape index	\tilde{l}	$\frac{2}{\pi} \arctan \left(-\frac{1}{2\tilde{e}} \right)$	$(-1, 1)$	$p(\tilde{l}) = \frac{\pi}{2} \frac{ \cos(\frac{\pi}{2}\tilde{l}) }{ \sin^3(\frac{\pi}{2}\tilde{l}) } \left[1 + 2 \cot^2 \left(\frac{\pi}{2}\tilde{l} \right) \right]^{-\frac{3}{2}}$
fractional anisotropy	\tilde{f}_a	$\frac{1}{\sqrt{2}} \frac{\tilde{\lambda}_1 - \tilde{\lambda}_2}{\sqrt{\tilde{\lambda}_1^2 + \tilde{\lambda}_2^2}}$	$(0, 1)$	$p(\tilde{f}_a) = \frac{2\tilde{f}_a}{(1 - \tilde{f}_a^2)^{\frac{1}{2}} (1 + \tilde{f}_a^2)^{\frac{3}{2}}}$
fractional isotropy	\tilde{f}_i	$\frac{1}{\sqrt{2}} \frac{\tilde{\lambda}_1 + \tilde{\lambda}_2}{\sqrt{\tilde{\lambda}_1^2 + \tilde{\lambda}_2^2}}$	$(-1, 1)$	$p(\tilde{f}_i) = \frac{1}{(2 - \tilde{f}_i^2)^{\frac{3}{2}}}$
gradient	\tilde{g}	$\frac{g}{\sigma_1^2}$	$(0, \infty)$	$p(\tilde{g}) = e^{-\tilde{g}}$
derivative of gradient	\tilde{D}_g	$\frac{D_g}{\frac{1}{2}\sigma_1^2 \sqrt{3\sigma_2^2 - 2\sigma_1^2}}$	$(-\infty, \infty)$	$p(\tilde{D}_g) = \frac{2}{\sqrt{\pi}} \int_0^\infty e^{-z^2 - \frac{\tilde{D}_g^2}{z^4}} \frac{dz}{z}$
Gaussian curvature	$\tilde{\kappa}_G$	$\frac{\tilde{d}}{(1 + \tilde{g})^2}$	$(-\infty, \infty)$	$p(\tilde{\kappa}_G) = \begin{cases} -\int_{-\infty}^{\tilde{\kappa}_G} \frac{2e}{\tilde{\kappa}_G} \sqrt{\frac{z}{3\tilde{\kappa}_G}} e^{-\sqrt{\frac{z}{\tilde{\kappa}_G}}} e^{4z} dz & \tilde{\kappa}_G < 0 \\ \int_{\tilde{\kappa}_G}^\infty \frac{2e}{\tilde{\kappa}_G} \sqrt{\frac{z}{3\tilde{\kappa}_G}} e^{-\sqrt{\frac{z}{\tilde{\kappa}_G}}} e^{4z} \left[1 - \operatorname{erf} \left(\sqrt{6z} \right) \right] dz & \tilde{\kappa}_G > 0 \end{cases}$
Curvedness	\tilde{c}	$\frac{1}{2} \sqrt{\tilde{\lambda}_+^2 + \tilde{\lambda}_-^2}$	$(0, \infty)$	$p(\tilde{c}) = \frac{16}{\sqrt{\pi}} \tilde{c} e^{-4\tilde{c}^2} D \left(\sqrt{2\tilde{c}} \right)$

Table 1. Definition of the normalised scalars as a function of the ordinary ones. The pdf's correspond to a Gaussian initial field and are independent of its power spectrum. Note that the values of σ_i may be pixel-dependent.

per cent for the three moments, with maximum errors less than 15 per cent for every pixel. Moreover, if we consider the error in $\sigma_i(\vec{x})$, including the contribution of both the signal and the noise, the average error becomes negligible (less than 0.1 per cent) whereas the maximum error is less than 1 per cent for every pixel and for the three moments considered. Therefore, for the considered work, we have used the simpler approach given by equation (16) to estimate the moments $\sigma_i(\vec{x})$ since the approximation works very well.

Regarding the effect of the mask, the smoothing of the masked map (with the pixels of the mask set to zero) reduces the discontinuity at its boundary. However, this smoothing strongly contaminates the pixels close to the boundary of the mask, and therefore the scalars calculated at those positions, which must be removed from the analysis. In order to do this, we will consider in our study only those pixels outside an extended mask that excludes also those pixels

significantly contaminated by the smoothing of the original mask.

This extended mask is obtained following the heuristic approach proposed by (Eriksen et al. 2004b). First, the original mask is smoothed with a Gaussian beam of dispersion 3 times the pixel size. Then, all those pixels above 0.991 are set to 1 (kept from the analysis) whereas those below this value are set to 0 (excluded from the analysis). Note that this way of constructing the mask is different and more conservative than the one presented in M05. In any case we have tested that both methods provide very similar results, but we have chosen the one of the present work due to its simplicity.

3 THE SIMULATIONS

In order to test the performance of the considered scalars to detect non-Gaussianity, we have generated different sets of Gaussian and non-Gaussian CMB simulations. In particular, we have used the Edgeworth expansion to simulate non-Gaussian CMB maps with a certain level of skewness or kurtosis. Although the simulations obtained in this way do not correspond to a particular physical model, they are, nonetheless, a useful tool to mimic some generic deviations of Gaussianity expected in realistic data. Indeed many physical motivated models, as well as contaminant emissions, will produce a certain level of these higher order moments on the CMB observations such as the quadratic potential inflationary model (which introduces skewness, Komatsu & Spergel 2001), cosmic strings (which generates kurtosis, Hobson et al. 1999, Barreiro & Hobson 2001) or point source residuals (which produce both, Argüeso et al. 2006).

The Edgeworth expansion of a one-point density function $f(y)$ can be expressed in terms of the Hermite polynomials (see e.g. Martínez-González et al. 2002 and references therein). Keeping only the first terms in the corresponding Hermite polynomials and considering only the skewness and kurtosis perturbations, we approximate the distribution function of our non-Gaussian simulations by the following two equations:

$$f_S(z) = \frac{e^{-\frac{z^2}{2}}}{\sqrt{2\pi}} \left\{ 1 + \frac{S}{6} [z(z^2 - 3)] \right\} \quad (17)$$

$$f_K(z) = \frac{e^{-\frac{z^2}{2}}}{\sqrt{2\pi}} \left[1 + \frac{K}{24} (z^4 - 6z^2 + 3) \right] \quad (18)$$

where S and K denote skewness and kurtosis, respectively. These distribution functions are not always well defined, because they can become negative even for relatively small values of S or K . To avoid this problem we set the function to zero when it becomes negative and then renormalise it to unit area. Note that for values of S , $K \lesssim 1$, the zeroes of the function always appear in the tails of the distribution, so the renormalization value is close to 1.

Our test CMB simulations have been produced with the aid of the HEALPix package (Górski et al. 2005), using a resolution of $N_{side} = 256$ (which corresponds to a pixel of 13.7 arcminutes). Following Martínez-González et al. (2002), we have generated non-Gaussian Edgeworth simulations as follows. First we produce simulations of white noise with a distribution given by equations (17) and (18) for different values of S and K (considering also the case $S = K = 0$, which corresponds to a Gaussian distribution). These maps are then convolved with a Gaussian beam of FWHM=23 arcmin. Finally we renormalize the power spectrum of the resulting map to the desired CMB power spectrum. In particular, we have used the power spectrum given by the best-fit model to the 1-year WMAP data (Spergel et al. 2003) convolved with a Gaussian beam of FWHM=33 arcmin. The C_ℓ 's for this model were generated using CMBFAST (Seljak & Zaldarriaga 1996).

Note that as a consequence of the first beam convolution and the introduction of correlations in the temperature maps, the simulated field does not longer follow the expressions given by equations (17) and (18) and, in particular,

the levels of the injected S and K have been significantly reduced. Nevertheless, the important point is that this process generates non-Gaussian simulations with the desired power spectrum and whose final level of S and K can be controlled through the values of the original injected skewness and kurtosis. The upper part of table 2 gives the mean and standard deviation of the final skewness and kurtosis obtained from 1000 simulations for different injected values of S and K . Note that the reduction in the level of K is more important than the one in S .

As a first step to test the power of the scalars to detect non-Gaussianity we have applied our method to these three sets of ideal simulations: Gaussian, injected skewness ($S = 0.08$) and injected kurtosis ($K=0.4$) (section 4.1). Note that we have chosen to inject in the simulations only skewness or kurtosis to discriminate better the effect of each of these higher moments in the Gaussianity test. We remark that the particular values of S and K have been selected to allow for a good comparison between the performance of the different scalars (although consistent results were obtained using different values of these parameters).

However, in a realistic experiment, the data will be contaminated by some level of instrumental noise. Moreover, some regions of the sky may be severely contaminated by different astrophysical emissions and thus will be excluded from the analysis. Therefore, we have also analysed a set of realistic simulations that take into account these problematics (section 4.2). In addition to the CMB signal, our realistic simulations contain anisotropic Gaussian noise at the level expected in the Q+V+W combined map of the 4-year WMAP data and has been masked using the Kp0 mask of the WMAP team (Bennett et al. 2003b). As explained in the previous section, in order to reduce the discontinuities produce by the noise and the mask, we have further smoothed the simulations with a Gaussian beam of FWHM=33 arcminutes. Finally, following the procedure explained in section 2, we have constructed an extended mask that excludes from the Gaussian analysis those pixels contaminated by the original mask due to this extra filtering. Note that whereas the Kp0 mask covers approximately a 23.9% of the full sky, the extended Kp0 mask used in the Gaussian analysis excludes a total of 31.7% of the pixels.

For the realistic case, we have considered also three different sets of simulations: Gaussian, injected skewness and injected kurtosis. Obviously, due to the presence of noise and mask, it is more difficult to distinguish between different models. Therefore, in order to obtain a meaningful comparison between the power of the different scalars, we have chosen in this case higher values for the injected skewness ($S = 0.2$) and kurtosis ($K = 1.6$). The lower part of table 2 gives the corresponding mean and dispersion of the final skewness and kurtosis obtained from 1000 realistic simulations.

4 RESULTS

In the present section we have tested the performance of the different normalised scalars² to detect generic devia-

² Note that in this section, even if not said explicitly, when talking about scalars we will always refer to the normalised quantities.

Table 2. Mean and standard deviation of the skewness and kurtosis of maps simulated through the Edgeworth expansion for different injected values of S and K . The results have been obtained from 1000 simulations for each considered case.

	injected S	injected K	$\langle S \rangle$	σ_S	$\langle K \rangle$	σ_K
Ideal	0.00	0.00	-1.41×10^{-3}	3.23×10^{-2}	-9.02×10^{-3}	3.38×10^{-2}
	0.08	0.00	1.18×10^{-2}	3.20×10^{-2}	-8.08×10^{-3}	3.45×10^{-2}
	0.00	0.40	8.97×10^{-4}	3.45×10^{-2}	5.82×10^{-3}	3.62×10^{-2}
Realistic	0.00	0.00	2.82×10^{-4}	4.59×10^{-2}	-1.20×10^{-2}	5.48×10^{-2}
	0.20	0.00	2.21×10^{-2}	4.63×10^{-2}	-1.17×10^{-2}	5.33×10^{-2}
	0.00	1.60	-1.55×10^{-3}	4.55×10^{-2}	1.78×10^{-2}	5.21×10^{-2}

tions from non-Gaussianity using the sets of simulations previously described. In order to discriminate between the Gaussian and non-Gaussian cases, we have applied the well-known Kolmogorov-Smirnov (KS) test (e.g. Von Misses 1964) for each scalar. Given a scalar map, the test simply consists on obtaining the maximum distance between the empirically constructed cumulative function of the scalar map and the expected theoretical one corresponding to the null hypothesis (in our case that the underlying temperature map is Gaussian). In most cases this theoretical cumulative function can be obtained, either analytically or numerically, for each scalar from the pdf's given in table 1 (see appendix D for the analytical expressions of the cumulative functions of some scalars). Nonetheless, for two scalars (derivative of the gradient and Gaussian curvature) with complicated pdf's we found more convenient to obtain it simply as the average of the empirically constructed cumulative function of the 1000 Gaussian simulations.

For a given normalised scalar, the procedure is as follows. First we obtain the scalar map for our sets of Gaussian and non-Gaussian simulations. Then we construct the probability distribution of KS distances for each set of simulations. Afterwards we compare the Gaussian case with the corresponding non-Gaussian one (either ideal or realistic). The capability of the scalar to discriminate between both cases is quantified by obtaining the power p of the test at a given significance level α (see e.g. Cowan 1998). For a significance level α , we reject the null hypothesis if a simulation has a KS distance, d_{KS} , higher than that of a fraction $1 - \alpha$ of the Gaussian simulations. Therefore α defines a critical value d_c below (above) which we accept (reject) the null hypothesis. p is defined as the fraction of simulations of the alternative hypothesis with values of d_{KS} higher than d_c . Therefore, for a fixed value of α , a large value of p indicates that there is a small overlap between both probability distributions and thus the models can be distinguished. We have performed this study for all the considered scalars, as well as for the normalised temperature map, using the ideal and realistic sets of Gaussian and non-Gaussian simulations described in the previous section. The power of the scalars to discriminate between the different cases has then been compared.

4.1 Ideal case

As a first step, we have applied our Gaussian analysis to the three types of ideal CMB simulations described in table 2: Gaussian, skewness ($S = 0.08$) and kurtosis ($K = 0.4$). The

left panel of figure 1 shows the probability distribution of KS distances, $p(d_{KS})$, obtained from the temperature maps of 1000 Gaussian (solid), skewness (dashed) and kurtosis (dotted) CMB simulations. As expected from the small values of skewness and kurtosis present in the non-Gaussian simulations (table 2), the three curves completely overlap and thus the temperature distribution cannot discriminate between the different cases. Similarly, we have performed the KS test for each of the normalised scalars. Figure 2 shows the KS distance probability distribution of the normalised Laplacian, shape index, derivative of the gradient and fractional anisotropy. As seen in the figure, the Laplacian (top left) is able to discriminate very well between the Gaussian and both non-Gaussian models, since the probability distribution corresponding to the Gaussian case overlaps only slightly with the ones of the non-Gaussian simulations. The shape index (top right) and the derivative of the gradient (bottom left) are able to discriminate between the Gaussian and skewness simulations but the power of the test is lower for the kurtosis case. For the fractional anisotropy the probability distribution of the skewness simulations completely overlap with the Gaussian one, whereas the case of the kurtosis simulations is clearly separated.

Table 3 gives the power of the normalised temperature and the different normalised scalars to discriminate between the ideal Gaussian and skewness ($S = 0.08$) simulations for two significance levels ($\alpha = 0.01, 0.05$). The same information is also given for the ideal kurtosis ($K = 0.4$). We remark that the distortion and the shear have the same discriminating power since they are related through a strictly monotonous function. Thus we present the results only for the distortion.

As seen in table 3, the best scalars at detecting an excess of skewness are the fractional isotropy, the Laplacian and the shape index, all of them with $p > 99$ per cent for $\alpha = 0.05$, and also the derivative of the gradient, with a slightly lower power. Regarding the kurtosis simulations, the scalars that perform better are the Laplacian, the fractional anisotropy, the determinant and the curvedness, which all give values of the power ≥ 99.7 per cent for $\alpha = 0.05$. Note that the performance of the temperature to discriminate between the Gaussian and non-Gaussian models is very poor and many of the scalars perform better than the temperature, especially for the kurtosis case.

Given the very small amount of skewness and kurtosis injected in the temperature distribution of the non-Gaussian simulations (see table 2), it is not surprising that we can not discriminate between the different considered models using this quantity. However, we may wonder why some of the

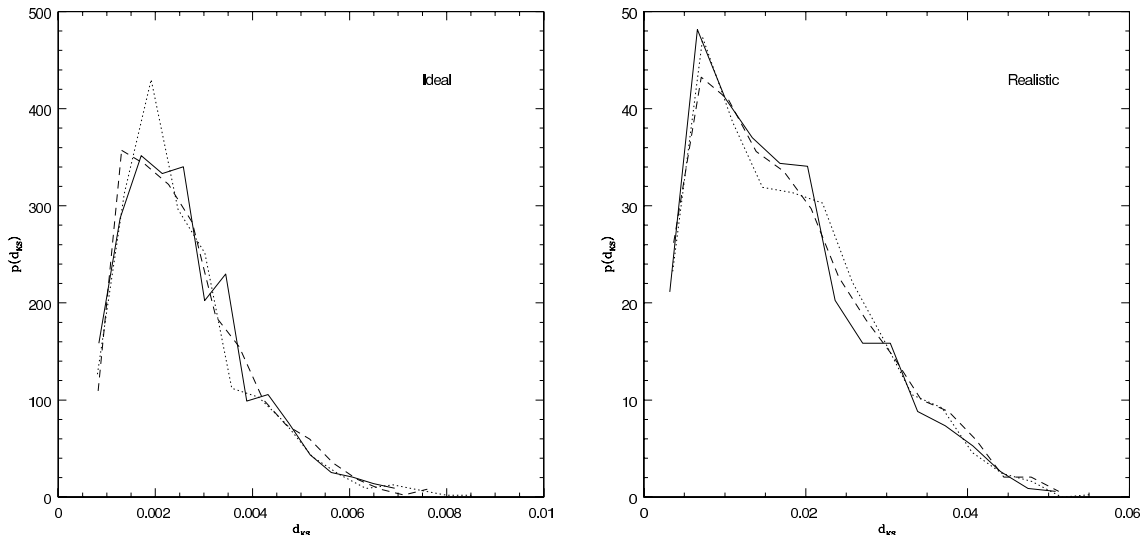


Figure 1. Probability distributions of the KS distances $p(d_{KS})$ corresponding to the CMB normalised temperature maps, each of them obtained from 1000 simulations, for the ideal (left panel) and realistic (right panel) cases. The different lines correspond to the Gaussian (solid), skewness (dashed) and kurtosis (dotted) sets.

Table 3. Power, p , of the KS test at two different significance levels ($\alpha = 0.05, 0.01$) to discriminate between the Gaussian and non-Gaussian simulations for the normalised temperature and the normalised scalars. We show the results for both the ideal and realistic cases.

	Ideal case				Realistic case			
	S=0.08		K=0.40		S=0.20		K=1.60	
	$\alpha = 0.05$	$\alpha = 0.01$						
Temperature	7.5	1.9	8.4	2.3	5.3	1.3	4.6	1.5
Laplacian	99.8	98.1	99.8	99.0	99.3	96.7	99.9	98.8
Greatest eigenvalue	92.7	80.1	92.7	75.2	69.7	41.6	75.6	51.2
Lowest eigenvalue	92.0	78.3	93.1	76.6	73.1	46.9	78.1	56.5
Determinant	5.9	0.7	99.7	99.2	4.3	0.4	99.5	98.4
Distortion	5.3	0.8	73.4	48.7	4.3	0.6	48.6	25.7
Ellipticity	95.2	86.9	61.1	27.8	98.4	91.9	78.0	32.9
Shape index	99.5	97.9	89.3	63.2	99.1	97.1	96.1	77.3
Fractional anisotropy	6.4	2.4	99.7	98.9	6.5	1.8	100.0	100.0
Fractional isotropy	99.9	98.8	91.2	73.6	99.7	97.9	93.8	72.4
Gradient	8.7	2.1	66.7	43.1	4.6	1.2	72.4	51.6
Derivative of the gradient	98.3	92.4	42.5	10.2	99.7	98.7	74.8	57.0
Curvedness	6.3	1.2	99.8	99.3	5.5	0.9	95.0	85.6
Gaussian curvature	6.8	1.7	7.4	1.9	7.9	1.8	61.2	37.5

scalars are able to detect the non-Gaussianity. The reason is that this non-Gaussianity can be amplified in certain scalar maps. To illustrate this point, we have calculated the mean value and dispersion of the skewness of the Laplacian for the ideal Gaussian and skewness simulations, finding the values $(-0.86 \pm 4.03) \times 10^{-3}$, and $(2.89 \pm 0.41) \times 10^{-2}$, respectively. Comparing these values with those given in the upper part of table 2, that were obtained directly from the CMB temperature simulations, it can be seen that the skewness has been significantly enhanced in the Laplacian map. Therefore, for the considered case, the non-Gaussianity can be much more easily detected using the Laplacian than the temperature map. An analogous argument holds for the kurtosis simulations. In this case we obtained values for the kurtosis of the

Laplacian map of $(0.01 \pm 7.87) \times 10^{-3}$, and $(7.11 \pm 0.86) \times 10^{-2}$ for the ideal Gaussian and kurtosis simulations, respectively.

From the results of table 3 it also becomes clear that one scalar can be very good at discriminating one type of non-Gaussianity whereas its performance can be very poor for a different type. This points out again the fact that it is not a trivial task to find a unique Gaussianity test which is optimal in all cases and motivates the investigation of a relatively large set of scalars.

We may wonder how our method compares with other Gaussianity tests proposed in the literature. For instance, techniques based on spherical wavelets have provided to be a very useful tool to study the Gaussianity of the CMB (e.g. Barreiro et al. 2000, Cayón et al. 2001, Martínez-González et al. 2002, Vielva et al. 2004).

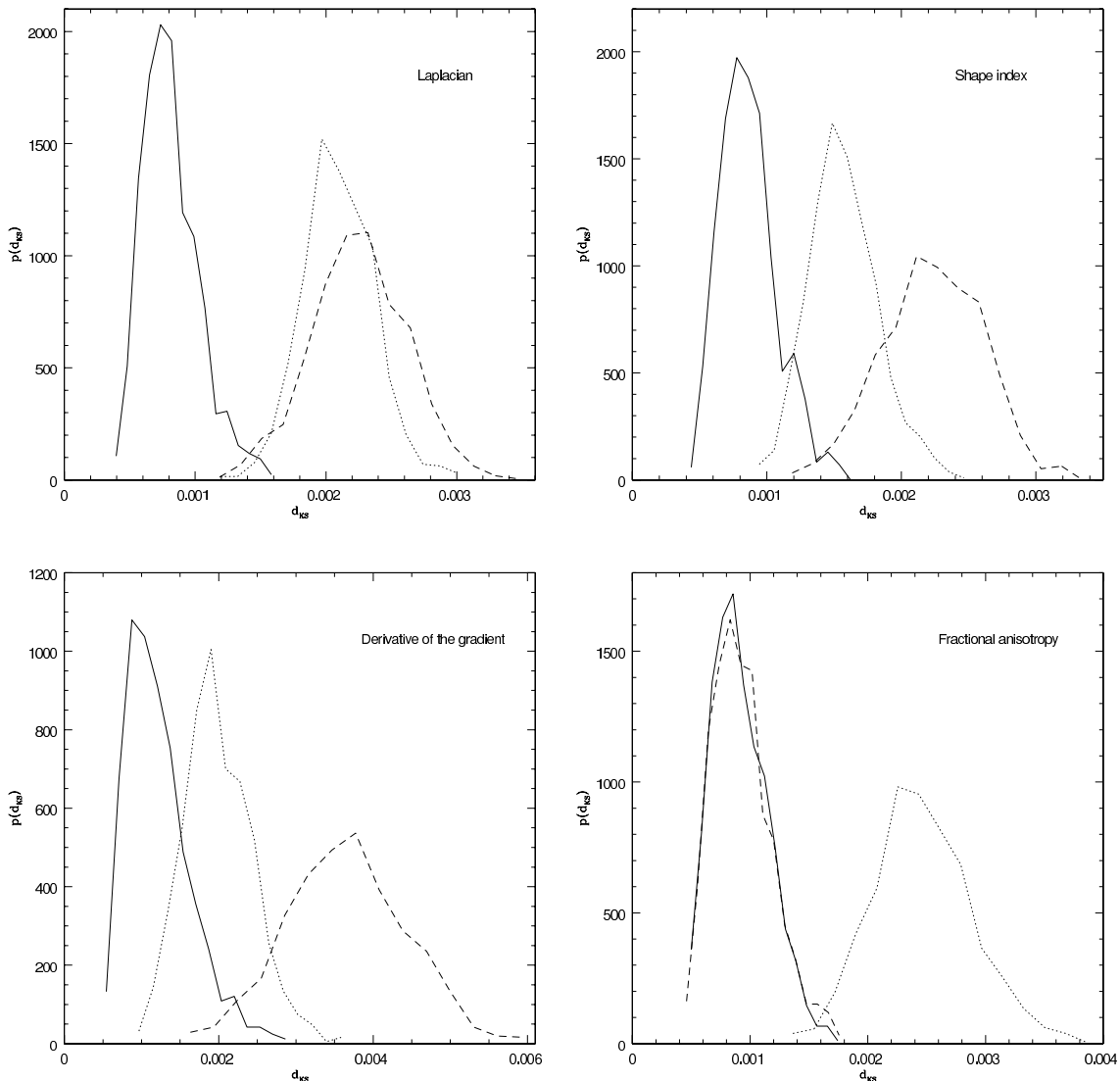


Figure 2. Probability distribution of the Kolmogorov-Smirnov distances corresponding to the normalised Laplacian (top left panel), the shape index (top right panel), the derivative of the gradient (bottom left panel) and the fractional anisotropy (bottom right panel) of the ideal simulations. Each probability distribution is obtained from 1000 simulations for the different considered cases: Gaussian (solid line), injected skewness (dashed), and injected kurtosis (dotted).

In particular, Martínez-González et al. (2002) studied and compared the performance of the spherical Mexican hat wavelet and the Spherical Haar Wavelet using simulations generated through the Edgeworth expansion. Unfortunately, that work is not directly comparable to the analysis that we present, since there are several differences between the used methods and simulations, most notably the fact that they use the Fisher discriminant to separate between Gaussian and non-Gaussian distributions and the different levels of injected skewness and kurtosis. Nonetheless, by looking at their results in table 2 we can get some insight on the comparative performance of the scalars versus the spherical wavelets. In particular, it is clear that the best of our scalars would outperform the spherical Haar wavelet, whereas it seems that they would provide comparable levels of detection to those of the spherical Mexican hat wavelet.

4.2 Realistic case

We have also applied our technique to the realistic CMB simulations described in section 3. As in the ideal case, we have considered three sets of simulations (see table 2): Gaussian, injected skewness ($S = 0.2$) and injected kurtosis ($K = 1.6$). As already explained, we have increased the levels of non-Gaussianity in these simulations to allow for a better comparison between the different scalars in the presence of noise and a mask.

As for the ideal case, we find that the probability distributions of KS distances, $p(d_{KS})$, corresponding to the Gaussian and non-Gaussian simulations completely overlap for the normalised temperature (see right panel of Fig. 1). Regarding the scalars, we give in Fig. 3 the KS distance probability distributions of the normalised Laplacian, shape index, derivative of the gradient and fractional anisotropy, for the three sets of realistic simulations. The results are

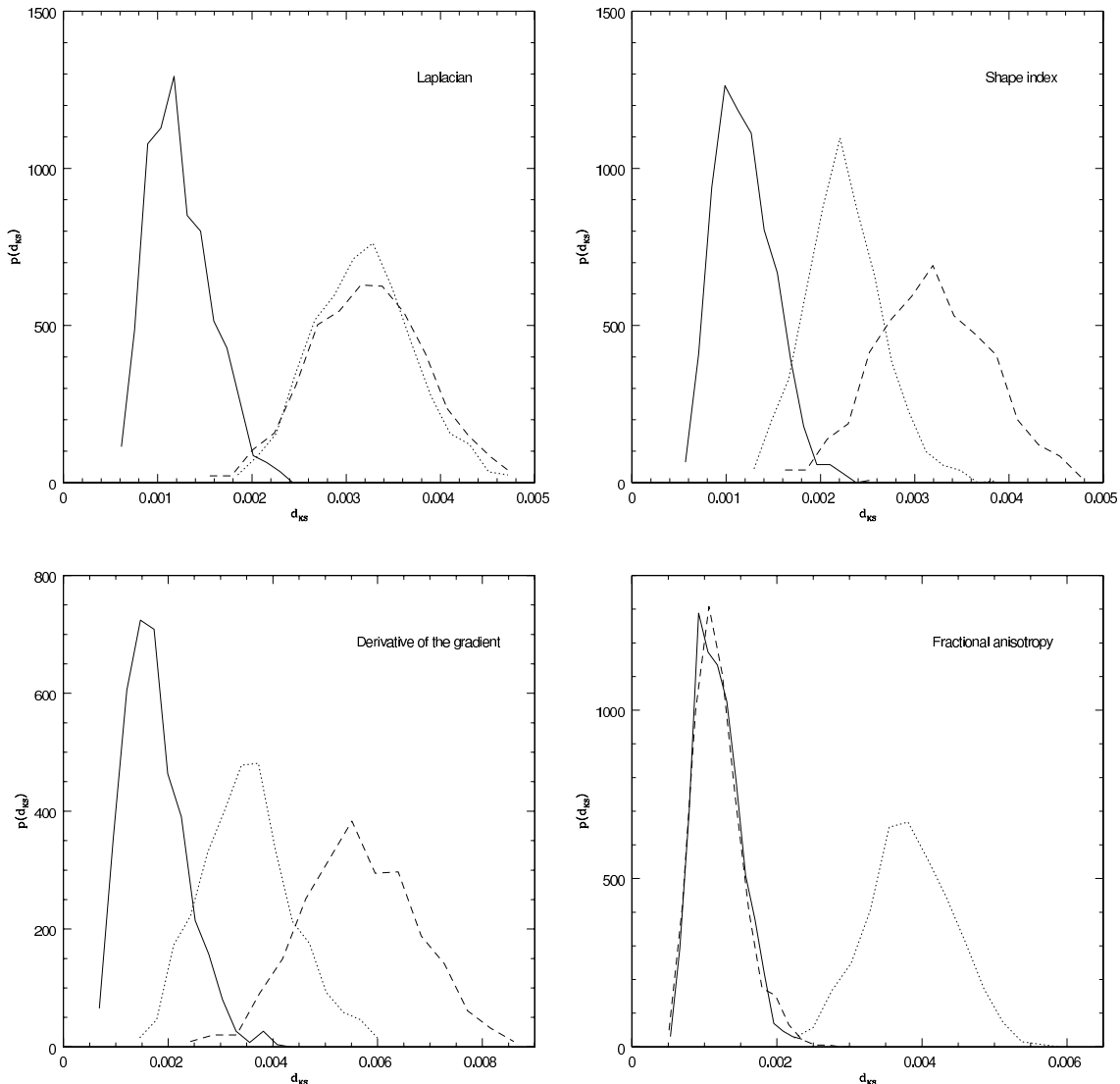


Figure 3. Probability distributions of the KS distances, corresponding to the Laplacian (top left panel), the shape index (top right panel), the derivative of the gradient (bottom left panel) and the fractional anisotropy (bottom right panel) of the realistic simulations. Each probability distribution is obtained from 1000 simulations and the different lines correspond to the Gaussian case (solid line), injected skewness (dashed) and injected kurtosis (dotted).

qualitatively similar to those of the ideal case: the Laplacian can distinguish reasonably well the Gaussian case from both types of non-Gaussian simulations, the shape index and the derivative of the gradient are good at detecting the skewness case whereas the fractional anisotropy can discriminate only between the Gaussian and kurtosis simulations.

The results regarding the power of the test at two different levels of significance ($\alpha = 0.01, 0.05$) for the temperature and the considered scalars are given in table 3 for both the skewness and kurtosis realistic cases. The comparative performance of the different scalars is very similar to that obtained for the ideal case, although some scalars seem to be more affected by the noise than others. In particular, for the skewness case, the fractional isotropy, the Laplacian and the shape index give again high values of the power, but they are outperformed by the derivative of the gradient, that seems more robust under realistic conditions. Regarding the kurtosis simulations, the fractional anisotropy, the Lapla-

cian and the determinant perform again very well, whereas the curvedness is more affected by the presence of noise and gives a somewhat lower discriminating power.

5 CONCLUSIONS

M05 introduced a set of normalised scalars constructed on the sphere from the covariant derivatives of the temperature field. The possible use of these quantities for a Gaussian analysis of the CMB was also proposed. In the present work, following M05, we have presented a Gaussian analysis for CMB data based on the statistical properties of the normalised scalars. The comparative performance of the different scalars has been tested using Gaussian and non-Gaussian simulations generated through the Edgeworth expansion. In particular, we have used two different types of non-Gaussian simulations: with injected skewness and with injected kur-

tosis. In addition we have considered an ideal case (where noiseless all-sky simulations were constructed) and a realistic case (containing anisotropic noise and a mask).

In order to quantify the power of the different scalars to detect non-Gaussianity we have used the Kolmogorov-Smirnov test. We find that, in most cases, the scalars amplify the non-Gaussianity present in the temperature map and produce higher detections than those obtained directly with the temperature. In particular, the best scalars to discriminate between the Gaussian and injected skewness cases are the Laplacian, the fractional isotropy, the shape index and the derivative of the gradient. For the kurtosis case, the highest powers are found for the determinant, the fractional anisotropy, the Laplacian and the curvedness. Note that some scalars can be very good at detecting one type of non-Gaussianity but perform very poorly for discriminating the other type.

In future works, we expect to test the discriminating power of these quantities using physically motivated non-Gaussian models such as the quadratic potential model (Liguori, Matarrese & Moscardini 2003) and also apply them to the analysis of the WMAP data.

ACKNOWLEDGMENTS

The authors thank P. Vielva and H. K. Eriksen for their useful comments, and also R. Marco for the computational support. CM thanks the Spanish Ministerio de Educación y Ciencia (MEC) for a predoctoral FPI fellowship. We acknowledge partial financial support from the Spanish MEC project ESP2004-07067-C03-01. This work has used the software package HEALPix 2.00 (Hierarchical, Equal Area and iso-latitude pixelization of the sphere, <http://www.eso.org/science/healpix>), developed by K.M. Górski, E.F. Hivon, B.D. Wandelt, A.J. Banday, F.K. Hansen and M. Barthelmann. We acknowledge the use of the software package CMBFAST (<http://www.cmbfast.org>) developed by U. Seljak and M. Zaldarriaga.

REFERENCES

- Aghanim N., Kunz M., Castro P.G., Forni O., 2003, *A&A*, 406, 797-816
- Argüeso F., Sanz J.L., Barreiro R.B., Herranz D., González-Nuevo J., 2006, submitted to *MNRAS*.
- Barreiro R.B., Sanz J.L., Martínez-González E., Cayón L. & Silk J., 1997, *ApJ*, 478, 1
- Barreiro R.B., Hobson M.P., Lasenby A.N., Banday A.J., Górski K.M., Hinshaw G., 2000, *MNRAS*, 318, 475
- Barreiro R.B., Martínez-González E. & Sanz J.L., 2001, *MNRAS*, 322, 411
- Barreiro R.B., Hobson M.P., 2001, *MNRAS*, 327, 813
- Bartolo N., Komatsu E., Matarrese S., Riotto A., 2004, *Phys.Rept.*, 402, 103
- Basser P.J., Pierpaoli C., 1996, *J Magn Reson Med B*, 111, 209-219
- Bennett, C.L. et al, 2003a, *ApJS*, 148, 1
- Bennett, C.L. et al, 2003b, *ApJS*, 148, 97
- Benoit A. et al., 2003, *A&A*, 399, L19
- Beppu T., Inoue T., Shibata Y., Kurose A., Arai H., Ogasawara K., Ogawa A., Nakamura S. & Kabasawa H., 2003, *Journal of Neuro-Oncology*, 63, 2, 109-116
- Bond J.R. & Efstathiou G., 1987, *MNRAS*, 226, 655
- Cabella P., Hansen F.K., Marinucci D., Pagano D. & Vittorio N., 2004, *Ph.RvD*, 69, 6, id. 063007
- Cabella P., Liguori M., Hansen F.K., Marinucci D., Matarrese S., Moscardini L. & Vittorio N., 2005, *MNRAS*, 358, 684
- Cayón L., Sanz J.L., Martínez-González E., Banday A.J., Argüeso F., Gallegos J.E., Górski K.M., Hinshaw G., 2001, *MNRAS*, 326, 1243
- Cayón L., Jin J., Treaster A., 2005, *MNRAS*, 362, 826
- Chiang L. Y., Naselsky P.D., Verkhodanov O.V., Way M.J., 2003, *ApJ*, 590, L65
- Coles P., Dineen P., Earl J., Wright D., 2004, *MNRAS*, 350, 989
- Cowan G., 1998, 'Statistical data analysis', Oxford Univ. Press, Oxford
- Cruz M., Martínez-González E., Vielva P., Cayón L., 2005, *MNRAS*, 356, 29-40
- Cruz M., Tucci M., Martínez-González E. & Vielva P., 2006, *MNRAS*, 369, 57-67
- Cruz M., Cayón L., Martínez-González E., Vielva P. & Jin J., 2006, submitted to *MNRAS*, preprint (astro-ph/0603859)
- Doré O., Colombi S., Bouchet F.R., 2003, *MNRAS*, 344, 905
- Eriksen H.K., Hansen F.K., Banday A.J., Górski K.M., Lilje P.B., 2004a, *ApJ*, 605, 14
- Eriksen H.K., Novikov D.I., Lilje P.B., Banday A.J., Górski K.M., 2004b, *ApJ*, 612, 64
- Górski K.M., Hivon E. F., Wandelt B. D., Banday J., Hansen F. K. & Barthelmann M., 2005, *ApJ*, 622, 759
- Grainge K. et al., 2003, *MNRAS*, 341, L23
- Gurzadyan V.G. & Torres S., 1997, *A&A*, 321, 19
- Halverson N.W., et al., 2002, *ApJ*, 568, 38
- Hansen F.K., Cabella P., Marinucci D., Vittorio N., 2004, *ApJ*, 607, L67
- Hobson M.P., Jones A.W., Lasenby A.N., 1999, *MNRAS*, 309, 125
- Jin J., Starck J.-L., Donoho D.L., Aghanim N., Forni O., *EURASIP Journal on Applied Signal Processing (Special Issue on Applications of Signal Processing in Astrophysics and Cosmology)*, 2005, 15, 2470
- Koenderink, J., 'Solid Shape', 1990, MIT press, Cambridge, Massachusetts
- Komatsu E. & Spergel D.N., 2001, *Phys. Rev. D*, 63, 63002
- Komatsu E. et al., 2003, *ApJS*, 148, 119
- Kuo C.L. et al., 2004, *ApJ*, 600, 32
- Larson D.L., Wandelt B.D., 2004, *ApJ*, 613, L85
- Larson D.L., Wandelt B.D., 2005, *Phys. Rev. D.*, in press, preprint (astro-ph/0505046)
- Liguori M., Matarrese S., Moscardini L., 2003, *ApJ*, 597, 57L
- Magueijo J., Medeiros J., 2004, *MNRAS*, 351, L1
- Martínez-González E., Gallegos J.E., Argüeso F., Cayón L., Sanz J.L., 2002, *MNRAS*, 336, 22
- Mason B.S. et al., 2003, *ApJ*, 591, 540
- McEwen J.D., Hobson M.P., Lasenby A.N., Mortlock D.J., 2005, *MNRAS*, 359, 1583
- Monteserín C., Barreiro R.B., Sanz J.L. & Martínez-

- González E., 2005, MNRAS, 360, 9-23, (M05).
 Mukherjee P., Wang Y., 2004, ApJ, 613, 51
 Naselsky P.D., Doroshkevich A. G. & Verkhodanov O. V., 2004, MNRAS, 349, 695-704
 Novikov D., Colombi S. & Doré O., 2006, MNRAS, 366, 1201-1216
 Park C.G., 2004, MNRAS, 349, 313
 Seljak U., Zaldarriaga M., 1996, ApJ, 469, 437
 Spergel D. N. et al, 2003, ApJS, 148, 175
 Turok N., Spergel D. N., 1990, Phys. Rev. Letters, 64, 2736
 Vielva P., Martínez-González E., Barreiro R.B., Sanz J.L., Cayón L., 2004, ApJ, 609, 22
 Von Misses R., 'Mathematical theory of probability and statistics', 1964, (NY Academic Press)
 Werring D.J., Clark C.A., Barker G.J., Thompson A.J., Miller D.H., 1999, Neurology, 53, 1626-1632

APPENDIX A: CURVEDNESS

In this appendix we describe a new scalar, the curvedness (Koenderink 1990), that was not included in the study of M05. The curvedness, c , is a scalar defined in terms of the eigenvalues of the negative Hessian matrix of the field λ_1 and λ_2 by the following expression:

$$c = \frac{1}{2} \sqrt{\lambda_1^2 + \lambda_2^2} \quad (\text{A1})$$

By construction c is a positive quantity and is closely related to the curvature of the field. Note that points with larger values of λ_1 or λ_2 (positive or negative) will have larger values of c whereas it becomes zero for flat areas in the initial field (i.e. $\lambda_1 = \lambda_2 = 0$).

Similarly to the other scalars, the normalised curvedness is constructed replacing λ_1 and λ_2 by the normalised eigenvalues in equation (A1):

$$\tilde{c} = \frac{1}{2} \sqrt{\tilde{\lambda}_1^2 + \tilde{\lambda}_2^2} \quad (\text{A2})$$

When the initial field is Gaussian distributed, the probability distribution function of the curvedness is given by:

$$p(\tilde{c}) = \frac{16}{\sqrt{\pi}} \tilde{c} e^{-4\tilde{c}^2} D(\sqrt{2}\tilde{c}) \quad (\text{A3})$$

which is independent of the power spectrum of the field. D is the Dawson's function, defined by the integral equation:

$$D(x) = \int_0^x e^{-t^2} dt \quad (\text{A4})$$

The correlations of the normalised curvedness with the other normalised scalars are given in table A1.

APPENDIX B: FRACTIONAL ANISOTROPY

In this appendix we describe another interesting scalar, the fractional anisotropy f_a (Basser & Pierpaoli 1996). This quantity has been used in the analysis of medical images, including the investigation of some neural diseases like astrocytic tumors (Beppu et al. 2003) or multiple sclerosis (Werring et al. 1999).

f_a is defined as a function of the eigenvalues λ_1 and λ_2 :

$$f_a = \frac{1}{\sqrt{2}} \frac{\lambda_1 - \lambda_2}{\sqrt{\lambda_1^2 + \lambda_2^2}}. \quad (\text{B1})$$

which is proportional to the ratio of the distortion over the curvedness. By construction f_a is dimensionless and bounded, $0 < f_a < 1$. It encodes information about the asymmetry between the eigenvalues of the field.

The normalised fractional anisotropy \tilde{f}_a is given by

$$\tilde{f}_a = \frac{1}{\sqrt{2}} \frac{\tilde{\lambda}_1 - \tilde{\lambda}_2}{\sqrt{\tilde{\lambda}_1^2 + \tilde{\lambda}_2^2}}. \quad (\text{B2})$$

When the initial field is Gaussian, \tilde{f}_a will follow a probability density function given by

$$p(\tilde{f}_a) = \frac{2\tilde{f}_a}{(1 - \tilde{f}_a^2)^{\frac{1}{2}} (1 + \tilde{f}_a^2)^{\frac{3}{2}}} \quad (\text{B3})$$

which, by construction, is independent of the initial power spectrum of the field.

The correlations of \tilde{f}_a with the other normalised scalars are shown in table A1.

APPENDIX C: FRACTIONAL ISOTROPY

The fractional isotropy f_i is proportional to the ratio of the Laplacian over the curvedness:

$$f_i = \frac{1}{\sqrt{2}} \frac{\lambda_1 + \lambda_2}{\sqrt{\lambda_1^2 + \lambda_2^2}}. \quad (\text{C1})$$

By construction f_i is dimensionless and bounded, $-1 < f_i < 1$.

Following the usual construction, the corresponding normalised scalar \tilde{f}_i is given by:

$$\tilde{f}_i = \frac{1}{\sqrt{2}} \frac{\tilde{\lambda}_1 + \tilde{\lambda}_2}{\sqrt{\tilde{\lambda}_1^2 + \tilde{\lambda}_2^2}}. \quad (\text{C2})$$

For an original Gaussian field \tilde{f}_i follows the pdf:

$$p(\tilde{f}_i) = \frac{1}{(2 - \tilde{f}_i^2)^{\frac{3}{2}}}. \quad (\text{C3})$$

which is independent of the power spectrum of the field.

We include in table A1 the correlations of the normalised fractional isotropy with the rest of normalised scalars.

APPENDIX D: CUMULATIVE FUNCTIONS OF THE NORMALISED SCALARS

For some scalars, it is possible to obtain an analytical expression of its corresponding cumulative function by integrating the pdf's given in table 1, which are valid for the case of an initial Gaussian temperature field.

In particular, in table D1, we give the cumulative functions of the normalised Laplacian, shear, distortion, ellipticity, shape index, gradient, fractional anisotropy and fractional isotropy.

	$\tilde{\lambda}_1$	$\tilde{\lambda}_2$	$\tilde{\lambda}_+$	\tilde{d}	\tilde{y}	$\tilde{\lambda}_-$	\tilde{t}	\tilde{g}	\tilde{D}_g	$\tilde{\kappa}_G$	\tilde{c}	\tilde{f}_a	\tilde{f}_i
\tilde{c}	0.26	-0.26	0	0.26	0.61	0.62	0	0	0	0.21	1.00	-0.25	0
\tilde{f}_a	0.23	-0.23	0	-0.77	0.45	0.54	0	0	0	-0.69	-0.25	1.00	0
\tilde{f}_i	0.83	0.83	0.92	0	0	0	-0.99	0	-0.53	0	0	0	1.00

Table A1. Correlations of \tilde{c} , \tilde{f}_a and \tilde{f}_i with the rest of normalised scalars (obtained from Gaussian simulations).

Normalised scalar	Notation	Domain	cumulative
Laplacian	$\tilde{\lambda}_+$	$(-\infty, \infty)$	$F(\tilde{\lambda}_+) = \frac{1}{2} \left(1 + \operatorname{erf} \left(\frac{\tilde{\lambda}_+}{\sqrt{2}} \right) \right)$
shear	\tilde{y}	$(0, \infty)$	$F(\tilde{y}) = 1 - e^{-4\tilde{y}}$
distortion	$\tilde{\lambda}_-$	$(0, \infty)$	$F(\tilde{\lambda}_-) = 1 - e^{-\tilde{\lambda}_^2}$
ellipticity	\tilde{c}	$(-\infty, \infty)$	$F(\tilde{c}) = \begin{cases} \frac{1}{2} \frac{1}{\sqrt{1+8\tilde{c}^2}} & \tilde{c} < 0 \\ 1 - \left(\frac{1}{2} \frac{1}{\sqrt{1+8\tilde{c}^2}} \right) & \tilde{c} > 0 \end{cases}$
shape index	\tilde{t}	$(-1, 1)$	$F(\tilde{t}) = \begin{cases} \frac{1}{2} \left[1 - \frac{1}{\sqrt{1+2 \cot^2 \left(\frac{\pi}{2} \tilde{t} \right)}} \right] & \tilde{t} < 0 \\ \frac{1}{2} \left[1 + \frac{1}{\sqrt{1+2 \cot^2 \left(\frac{\pi}{2} \tilde{t} \right)}} \right] & \tilde{t} > 0 \end{cases}$
gradient	\tilde{g}	$(0, \infty)$	$F(\tilde{g}) = 1 - e^{-\tilde{g}}$
fractional anisotropy	\tilde{f}_a	$(0, 1)$	$F(\tilde{f}_a) = 1 - \sqrt{\frac{1-\tilde{f}_a^2}{1+\tilde{f}_a^2}}$
fractional isotropy	\tilde{f}_i	$(-1, 1)$	$F(\tilde{f}_i) = \frac{1}{2} \left(1 + \frac{\tilde{f}_i}{\sqrt{2-\tilde{f}_i^2}} \right)$

Table D1. Cumulative functions of some normalised scalars, for the case of an initial Gaussian field.